

Compact and High Performance Torque-Controlled Actuators and its Implementation to Disaster Response Robot

Yoshiki Kanemoto¹, Takahide Yoshiike², Masaaki Muromachi¹ and Masahiko Osada¹

Abstract—Applying robots in narrow and cluttered disaster environments such as oil refineries requires a slim body and a wide range of motion. It is also necessary to have abilities to absorb unexpected contact with the environment and to walk on scattered debris. In this paper we propose new compact and high performance torque-controlled actuators for legged robots to satisfy the above mentioned requirements. For axial compactness, torque sensors are designed as ring-shaped thin cylinders surrounding motors or gears with strain gauges for sensing. To achieve broad bandwidth of torque control, we introduced an analog differentiator circuit into an analog digital converter (ADC) board in order to suppress noise in the differential control of joint torque. We also propose methods to reduce torque ripple caused by the deformation of the harmonic drive gear and electromagnetic interference (EMI) from a motor and a motor driver. Finally, experiments of a collision with objects and movement on scattered debris were executed with a fully torque-controlled legged robot built with the proposed actuators.

I. INTRODUCTION

Today, legged robots are expected to enter dangerous disaster sites such as oil refineries or nuclear power plants to gather information and to respond to situations in place of humans. It is also desirable for such robots to have abilities to conduct daily maintenance and inspections in existing plant facilities. Existing plants are often quite narrow due to the installation of additional equipment over time. Therefore, robots are required to be slim. At the same time, robots are required to be flexible to absorb unexpected contact.

Actually, operators who remotely control robots in plants are worried about collisions due to the uncertainty of external sensors such as LIDARs. The ability to handle unexpected contacts contributes to increased success rates and reduces working time in disaster sites. To handle unexpected contact, whole-body joint torque control is one of the possible options. Robots with torque-controlled joints are able to react to contact anywhere on their body and are able to control contact forces if location of contact is identified. Therefore, a torque control system which can be mounted on slim legged robots is required.

Many recent robots have torque sensors installed in their joints. It is desirable to have a torque control system with high bandwidth and low tracking errors in order to produce very compliant behavior and precise execution of motion. Such a torque control system requires torque sensors with high accuracy and resolution. We also have to consider the size of actuators with torque sensors especially for

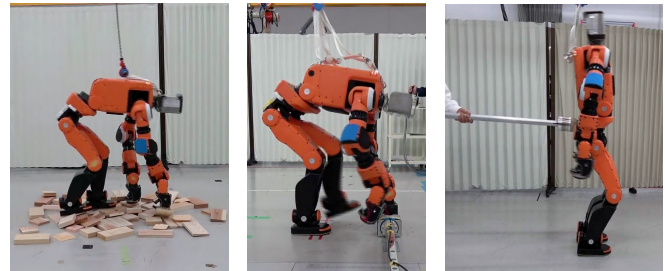


Fig. 1. Developed fully torque-controlled legged robot. (left) 0.2 m/s trotting upon scattered debris (middle) collision between swing limb and environment during 0.4 m/s trotting (right) push recovery while stomping

robots working in narrow environments. Hydraulic robots like the Atlas can estimate joint torque via a pressure sensor [1]. But estimated torque has relatively large uncertainty mainly caused by friction. Using a photo-interrupter [2][3] or an encoder [4][5] as a spring deflection sensor enables joint torque control. However, these optical sensors have a limitation when constructing slim robots because they require a relatively large deflection to ensure sufficient torque sensing resolution. Robots that utilize linear actuators can be extended to be torque-controlled by placing load-cells in-line [6][7]. Usually for legged robots, linear actuators require additional mechanisms to enable actuator movements to be rotational. Therefore, the amount of freedom for constructing a slim robot is limited. Strain gauges are often used as torque sensors attached to flexure elements [8][9][10][11] and have advantages to achieve compact actuators because strain gauges themselves are thin films and have sufficient sensitivity while they are attached to relatively stiff sensors [12]. Thus, we decided to focus on a system based on strain gauges to sense torque.

Nagasaka et al. [8] accomplished a 10 ms time constant of torque step response for a bi-manual mobile robot. Valkyrie has 70 Hz of torque tracking bandwidth [4]. Such torque control systems which have higher bandwidth amplify noise in sensor values. Therefore, it is important to improve the torque sensing signal-to-noise ratio (SNR). However, systems based on strain gauges often suffer from low a SNR. Lowering the stiffness of flexure elements usually improves SNR by increasing the deflection and strain for the same load. Usually flexure elements with a lower stiffness have a lower strength. Therefore, there is a limit to increase deflection by lowering stiffness[2]. Kuroki et al. developed strain gauges with a higher gauge factor [10] to get a better SNR.

Additionally, a false signal called a torque ripple is problematic while combining strain gauges with harmonic drive

¹ Honda R&D Co., Ltd, 8-1 Honcho, Wako, Saitama, Japan ² Honda Research Institute Japan Co., Ltd, 8-1 Honcho, Wako, Saitama, Japan

gears [13]. We also found another false signal caused by EMI from high voltage components such as motors and motor drivers.

The goal of this paper is to develop compact and high performance torque-controlled actuators that can be mounted on disaster response legged robots for narrow and cluttered environments. Actuators must be designed with special concern for control bandwidth, mechanical strength and compactness as these are essential for robust and precise execution at disaster sites. To realize such actuators based on strain gauges, we must solve the problems of mechanical design, SNR, torque ripple and EMI. In this paper we propose new methods to overcome these problems and show the design of actuators.

Whole-body control methods of torque-controlled legged robots have been advancing in recent years. They mainly solve a minimization problem of errors between desired and actual movements while considering an equation of motion and unilateral constraints like contacts [1][14][15][16].

We have developed a legged robot for disaster response which is equipped with the proposed actuators. The robot can pass through narrow passages 300 mm wide, climb up and down vertical ladders with safety cages 650 mm in diameter[17]. The robot is splash and dust proof. With high bandwidth joint torque control, we also realized robust movement on scattered debris, absorption of collisions of swing limbs while walking and push-recovery while stomping as shown in Fig. 1.

Section II presents the design of compact and high performance torque-controlled joints, the new methods for mechanical and electrical issues and the control system. Section III explains experimental setup and results using the actual robot. Finally, we conclude this paper in Section IV.

II. DEVELOPMENT OF COMPACT TORQUE-CONTROLLED JOINTS

The main requirements of actuators are determined by considering practical use in disaster sites. The main requirements are as follows:

- 1) Compactness
- 2) Wiring run inside of actuators
- 3) Torque tracking performance
- 4) Maximum speed and torque characteristics

For smooth operation in a narrow disaster environment with a wide reachable region, actuator units are required to be compact [17]. Compactness contributes to avoid interference with the environment, to extend operational range and to increase a spare space for cables and additional equipment. Cables must be inside a robot's body in order to improve splash-proofing and avoid snagging.

Hollow joints allow internal wiring with a reduced risk of kink and tangling. For functional flexibility, internal spaces of hollow joints should be determined based on cables volume.

High torque tracking performance is important for the stable execution of reference movement. Upon control loops

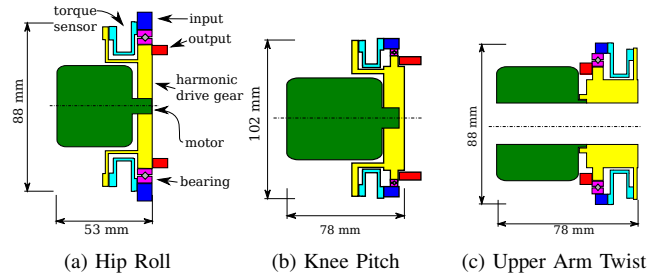


Fig. 2. Mechanical layout of proposed actuators. The design is characterized by a ring-shaped torque sensor placed outside of the motor or gear. This contributes to shorten the axial length and to enable a large central hole for internal wiring.

of each joint torque, we put a control layer which is responsible for executing whole-body movements. Torque tracking performance of each joint is necessary to ensure a robot operates properly. In order to absorb impacts between a robot's body and the environment, torque tracking performance also plays an important role. A higher response suppresses peak torque caused by external impacts. Resultant behaviors are also affected by the mechanical compliance of joints, inertia distribution and the decoupling effect of multiple spring-mass systems. These effects are changed by the pose of the robot and its grounding states. Therefore, we decided to test impact tolerance by impacting the tip of a swing limb with a fixed object on the floor while walking.

As specifications of actuators, it is necessary to satisfy speed and torque for required movements. Thus we cannot simply reduce the size of motors, gears, and torque sensors. Therefore, we optimized the shape of torque sensors and the geometric arrangements of components for compactness.

A. Mechanical Design

TABLE I. Peak torque requirement and typical dispersion of representative joints

	Hip Roll	Knee Pitch	Up. Arm Twist
peak torque (Nm)	180	280	95
$J_M(\text{kgm}^2)$	12.5×10^4	38.1×10^4	48.7×10^4
$K_S(\text{Nm/rad})$	29000	57000	29000
$K_t(\text{Nm/A})$	0.0719	0.0830	0.0439
reduction ratio	161	80	160
desired σ_τ (mNm)	10.6	190	10.4
desired $\sigma_{\dot{\tau}}$ (Nm/s)	76.0	136	12.0
actual σ_τ (mNm)	9.41	14.9	3.6
actual $\sigma_{\dot{\tau}}$ (Nm/s)	24.1	38.8	17.5
control freq. (Hz)	100	100	100

An actuator unit consists of a brushless DC motor, a harmonic drive gear and a torque sensor. The design of our torque-controlled actuator is characterized by a ring-shaped torque sensor placed outside of the motor or gear. This layout shortens the axial length of the actuators. Fig. 2(a) shows the structure of a hip-roll joint. A very short axial length is achieved by placing the torque sensor outside of the motor. Fig. 2(c) shows the twist joint of an upper arm. A large central hole is prepared for internal wiring. The axial length

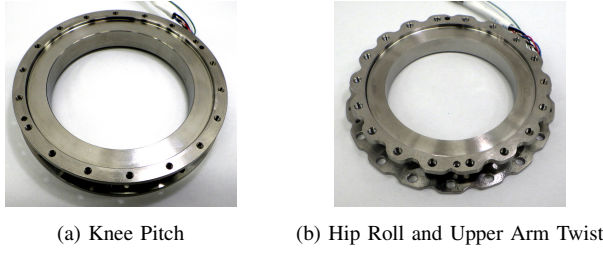


Fig. 3. Torque sensors

of the actuator is shortened by placing the torque sensor outside of the gear. 2(b) shows a knee-pitch joint.

We use strain gauges to measure joint torque. Even if we employ the highest resolution encoder currently available like a Renishaw optical sensor, shapes of torque sensors are limited such as long torsional bars or compliant spokes to ensure sufficient displacement. With these shapes, it is difficult to achieve compactness. Our sensors are designed to have a thin cylindrical flexure part with strain gauges attached and flanges to connect gears and links as shown in Fig. 3 and Fig. 5. The thickness of the flexure part is determined to be 0.15-0.2 mm in order to maximize the resolution while satisfying strength requirements.

B. Control and Differentiator Circuit

The block diagram of the joint torque control system is shown in Fig. 4. We chose a PD controller with a disturbance observer for the torque-control system because of its ease of tuning and its robustness [18][19]. These properties are preferable because the dynamics of the load side changes dynamically according to the pose and grounding state. We also employ a band rejection filter for each joint that has significant mechanical resonances.

Joint torque is measured using strain gauges arranged as Wheatstone bridge circuits with our custom ADC board. The ADC board has an analog differentiator circuit for measuring torque change rate in addition to an amplifier circuit to measure torque. The measured torque change rate $\dot{\tau}_{act}$ through an analog differentiator circuit has low noise compared to numerical differentiation for measured torque, because our system has a short sampling time (20 kHz) which amplifies noise on measured torque τ_{act} .

Control bandwidth is dominated by a derivative term which is calculated from the torque change rate. Low resolution or bad SNR of it leads to instability and wasted current consumption. Thus, clearness of the measured torque change rate contributes to broader control bandwidth.

The requirement of SNR is calculated by estimating average current consumption of steady state with feedback gains that will exert 100 Hz of control bandwidth in theory. The feedback gains can be calculated by assuming a two inertia system with a simple PD feedback loop. If we assume motor-side inertia J_M and load-side inertia J_L are connected by a spring with stiffness K_S , we can calculate proportional gain $K_{\tau P}$ and derivative gain $K_{\tau D}$ for arbitrary time constant T_τ and damping ratio ζ as follows.

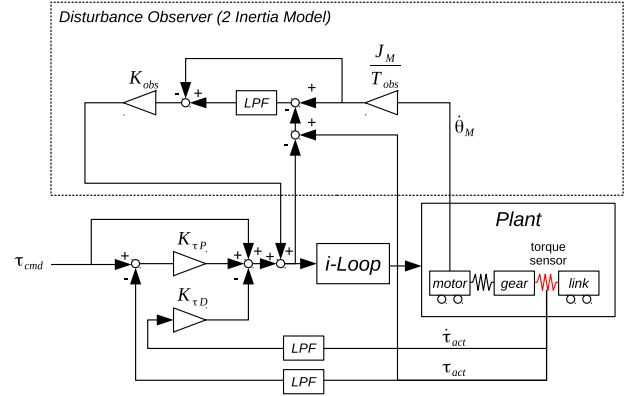


Fig. 4. Block diagram of joint torque control system. This system uses a PD controller with a disturbance observer. The torque change rate is generated by an analog differentiator circuit instead of numerical differentiation of torque. K_{obs} and T_{obs} are gain and time constant of disturbance observer respectively.

$$K_{\tau P} = \frac{J_M}{K_S T_\tau^2}, \quad K_{\tau D} = \frac{2J_M \zeta}{K_S T_\tau} \quad (1)$$

We can estimate the standard deviation of desired current σ_I from noise characteristics of sensors (σ_τ and $\sigma_{\dot{\tau}}$) as follows. K_t is the torque constant of the motor. R is the reduction ratio of the harmonic drive gear.

$$\sigma_I = \frac{1}{K_t R} (K_{\tau P} \sigma_\tau + K_{\tau D} \sigma_{\dot{\tau}}) \quad (2)$$

Desired σ_τ and $\sigma_{\dot{\tau}}$ are calculated and shown in Tab. I. We assume the desired average current consumption to be 0.1 A.

The actual σ_τ and $\sigma_{\dot{\tau}}$ are also shown in Tab. I. Most actual σ_τ and $\sigma_{\dot{\tau}}$ are less than the desired values except for the actual $\sigma_{\dot{\tau}}$ of the upper-arm-twist joint. However, it is not problematic for the performance of the robot because it does not affect its overall stability.

If we use numerical differentiation of measured torque as a torque change rate, the standard deviation of desired current σ_I can be estimated by substituting $\sigma_{\dot{\tau}}$ with $\sigma_\tau / 2\Delta t$ of equation (2). Δt is the duration of the control period.

$$\sigma_I = \frac{1}{K_t R} \left(K_{\tau P} \sigma_\tau + K_{\tau D} \frac{\sigma_\tau}{2\Delta t} \right) \quad (3)$$

The desired σ_τ estimated by equation (3) are 1.9 mNm for hip-roll, 3.4 mNm for knee-pitch and 0.3 mNm for upper-arm-twist. These values are much smaller than the desired σ_τ of the differentiator circuit. Therefore, we achieved a better SNR for the torque change rate compared to numerical differentiation by utilizing the differentiator circuit.

C. Reduction of Torque Ripple

At first, we built a full bridge system with 4 strain gauges on the surface of a torque sensor to measure shearing stress. However, our system encountered periodic noise in joint torque. This noise was synchronized with the angle

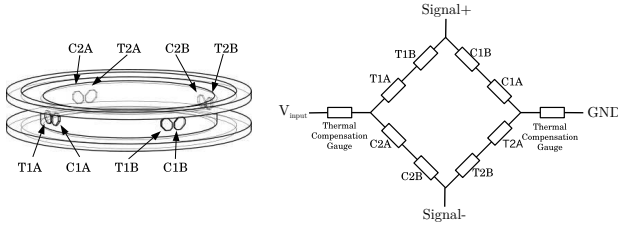


Fig. 5. 8 gauges are attached to cancel 180 degrees of periodical torque ripple. C1A, C1B, C2A and C2B are compressional gauges. T1A, T1B, T2A and T2B are tensional gauges. The excitation voltage is applied between V_{input} and GND. The voltage between Signal+ and Signal- is measured as the signal.

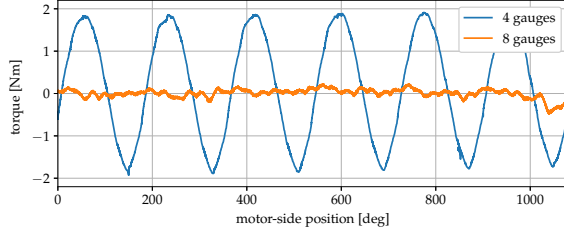


Fig. 6. 180 degree periodical torque ripple was observed (blue line). A method using 8 gauges suppressed the torque ripple to less than 1/10.

of the motor and was caused by the elliptical deformation of the harmonic drive gear which was connected directly to the torque sensor as reported by Kim et al. [13]. In the worst case, the amount of torque ripple was 4 Nm peak-to-peak at the knee-pitch joint. This amount was not ignorable especially for the inverse dynamic control of the swing leg.

Therefore, we attached 8 strain gauges to cancel the effect of deformation on measured torque as shown in Fig. 5. By placing strain gauges every 90 degrees, 180 degrees of periodical torque ripple was canceled. The 8 strain gauges reduced torque ripple to 0.1 Nm at the knee-pitch joint (Fig. 6).

D. Elimination of Electromagnetic Interference

At the hip-roll joint we observed false signals in torque change rate as shown in Fig. 7. These false signals are proportional to the current change rate. The motor of the hip-roll joint was placed inside of the torque sensor with narrow clearance surrounding it. These facts suggest the false signals were EMI induced by voltage from the motor's changing magnetic field according to Faraday's law of induction. The performance of joint torque control under EMI was much lower than others without it due to oscillation with a lower derivative gain as shown in Fig. 9.

We already used non-inductive foil strain gauges and twisted cables. Our torque sensor has a small terminal board attached to the flange of the sensor. We built the Wheatstone bridge circuit with this terminal board. However, the circuit probably became an EMI antenna because the size of the board was approximately one square centimeter.

We developed a special terminal board configuration to cancel EMI [20]. We changed the board from one-sided implementation to two-sided and found a configuration to

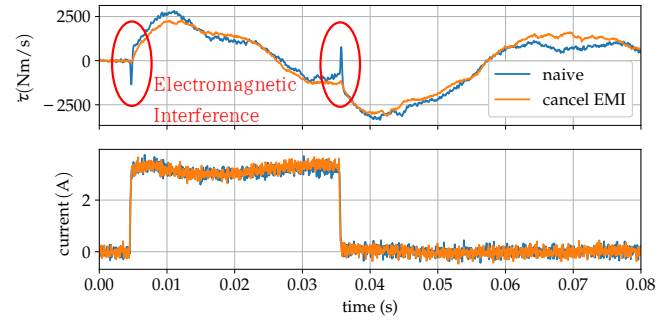


Fig. 7. The blue line shows EMI appeared in the torque change rate ($\dot{\tau}$) while applying step current to the motor. The orange line shows that EMI was eliminated by our cancel-EMI configurationT.

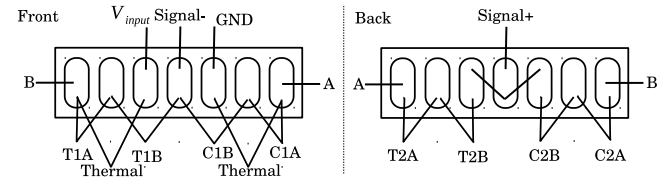


Fig. 8. Configuration of the terminal board in order to cancel EMI. The naming of terminals is shown in Fig. 5.

cancel voltage induced from spatially uniform change of magnetic field. Fig. 8 shows that wiring to compressional and torsional gauges are symmetrically arranged and are made to have similar loop-hole sizes. With this technique, EMI to compressional and torsional gauges is canceled out. Additionally, we placed the board as far as possible from the motor in parallel with the measured magnetic field induced from the motor.

As a result, EMI in the torque change rate was eliminated and the time constant of feedback control was improved from 6 ms to 1.5 ms as shown in Fig. 9.

III. EXPERIMENTS

A. Performance Tests of the Actuators

Performance tests of the actuators were conducted. Fig 10 shows the experimental setup of the actuator for the knee-pitch joint. The actuator unit was rigidly mounted to the stand. Load-side inertia coincided with the same joint of the actual robot. A 3.9 kg hammer was mounted to the end of a 600 mm bar which was fixed to another stand through a free rotational joint with an electrical brake. For an impact

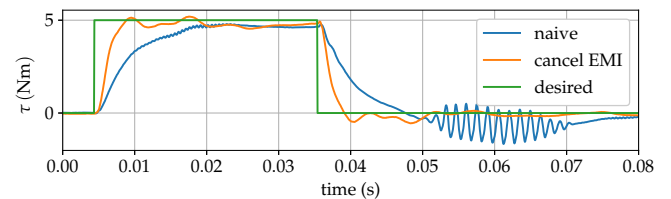


Fig. 9. Torque step response applied a special terminal board configuration to cancel EMI. Oscillation was observed by applying torque PD feedback under the presence of EMI.

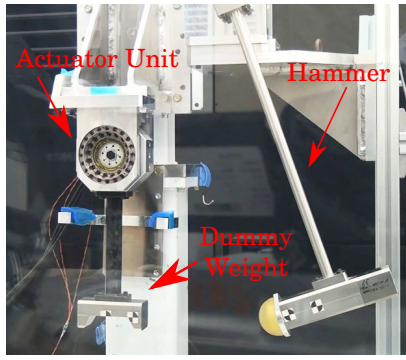


Fig. 10. An actuator unit of a knee-pitch joint, a load-side inertia and a hammer are prepared for the benchmark of a single joint. The load-side inertia is 0.14 kgm^2 . The hammer was 3.9 kg .

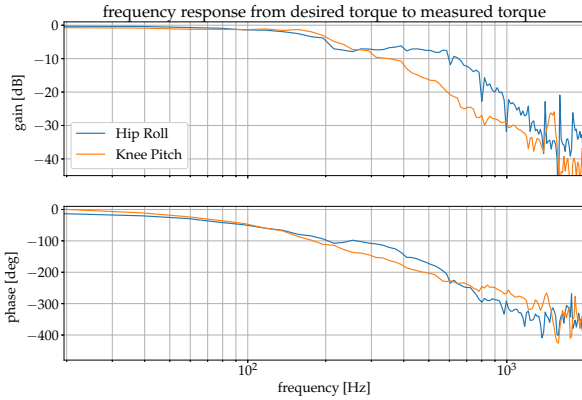


Fig. 11. Bode diagram of closed loop torque tracking.

test, the hammer started to move from an arbitrary height after the brake was released. The hammer was covered with urethane resin which had a hardness of A90 and a thickness of 5 mm . The Hardness and the thickness were tuned to have a collision time of $5\text{-}10 \text{ ms}$.

The joint torque controller was implemented on custom motor driver boards. The controller had an inner current loop and outer torque loop. The current loop ran at 80 kHz and was typically tuned to achieve a time constant of 0.1 ms for the current step response. The torque loop was running at 20 kHz as mentioned in II-B.

Before the impact test, we tuned the controller to achieve a broad control-bandwidth and with a small steady state error. Basically we used equation (1) for determining K_{TP} and K_{TD} . T_r , ζ and K_{obs} were determined experimentally to balance stability and performance. For the knee-pitch joint, we applied a band-rejection filter to suppress resonance possibly caused by low stiffness from the wave generator inside the harmonic drive gear [21].

A bode diagram of torque tracking performance is shown in Fig. 11. We achieved control-bandwidth over 100 Hz . The steady state error couldn't be zero because we did not fix the load-side of the joint. But the steady state error reached a theoretical value assuming infinite proportional gain and derivative gain.

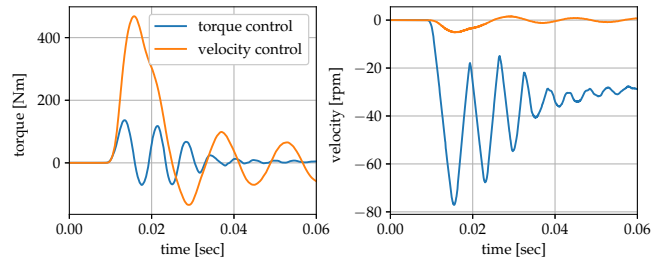


Fig. 12. Data from the impact test of the knee-pitch joint. The control methods were compared at the same experimental setup. The joint torque controller greatly lowered impact torque at the actuator.

Figure 12 shows the results of the impact test. The hammer was released from 40 degrees. An impact position was 290 mm below the actuator axis. For comparison, we use a proportional velocity controller which was tuned to a bandwidth of 1 kHz . The maximum torque at the actuator while using the velocity controller was 463 Nm . In the case of the torque controller, the maximum torque was only 136 Nm and the velocity was greatly increased in the opposite direction of the torque. This means the energy of impact was converted to kinetic energy of the load-side inertia instead of the potential energy of spring elements inside the joint.

B. Performance of Whole-Body Movement

Using the design and control methodology as already mentioned, we built 16 different actuators which consisted of 8 actuators for arms, 6 for legs and 2 for the body and installed them on a legged robot shown in Fig. 1. The robot was equipped with 30 torque controlled joints. The requirements and other design principles of the robot are described in [17].

We conducted experiments of bipedal and quadrupedal walking. Reference trajectories of these movements were calculated by the method shown in [22] and [23]. The controller to track reference whole-body motion consists of a state estimator, a desired acceleration calculator and an inverse dynamics solver. The state estimator estimates the states of the robot from an inertial measurement unit and actual joint positions [24]. The desired acceleration calculator calculates desired acceleration of movements in task-spaces mainly from position and velocity tracking errors. The inverse dynamics solver calculates joint torques by solving the weighted minimization of errors between desired and expected accelerations in task-spaces while satisfying centroidal dynamics and unilateral contact constraints. In the Darpa Robotics Challenge, several teams used similar approaches [1] [14] [15].

We evaluated bipedal forward walking varying speed up to 0.46 m/s with a step length of 350 mm , a step time of 750 ms and a double support time of 250 ms . Experiments were executed on a flat floor. Trajectories of zero moment point (ZMP) and center Of mass (COM) are shown in Fig. 13. The difference between the desired ZMP calculated from the inverse dynamics solver and the actual ZMP calculated from force torque sensors was small. This indicates that the high

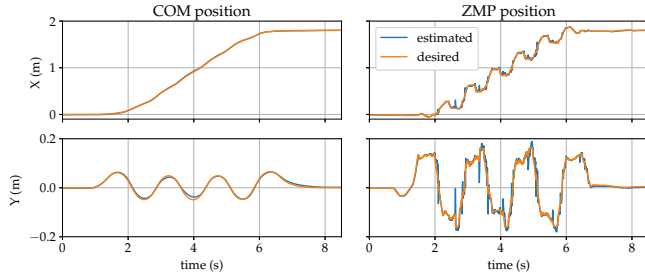


Fig. 13. COM and ZMP trajectory of bipedal walking at 0.46 m/s (7 steps). The desired COM is calculated by our motion generation algorithm[23]. The estimated COM is calculated by our state estimator which is described in [24]. The desired ZMP is calculated by an inverse dynamics solver described in section III-B. The estimated ZMP is calculated by force/torque sensors mounted below each ankle.

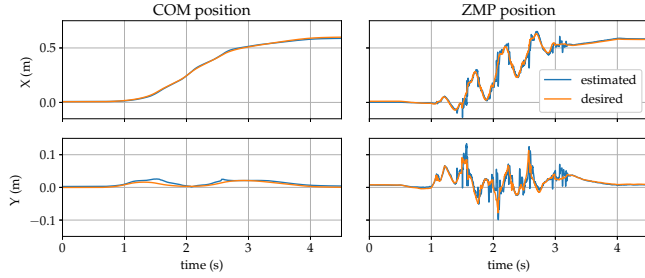


Fig. 14. COM and ZMP trajectories of trotting at 0.4 m/s (4 steps).

fidelity of the joint torque control system enables the control of contact forces and centroidal dynamics precisely. When the robot speed was more than 0.46 m/s, a tracking error of COM became larger and the robot fell down. However, we believe that there is much room for improvement because the position-controlled version of this robot is able to walk at 1.1 m/s on a flat floor [17].

We also tested forward trotting at a speed of 0.4 m/s with a step length of 200 mm, a step time of 500 ms and a double support time of 100 ms. Trajectories of ZMP and COM at 0.4 m/s trotting are shown in Fig. 14.

C. Whole-Body Disturbance Test

We also evaluated the robustness against disturbances like uneven terrain (unmodeled), collision with obstacles and push recovery. High fidelity torque-controlled legged robots are expected to keep stability with these disturbances.

Firstly, we tested quadruped walking on scattered debris in order to evaluate the robustness against uneven terrain. We randomly placed a lot of bricks and 10-30 mm high blocks on the floor. The maximum height of the piled debris was 60 mm. Bricks and blocks were not attached to the floor. The gait was 0.2 m/s trotting with a step length of 200 mm, a step time of 1000 ms and a double support time of 200 ms. The robot assumed that the floor was flat. COM and ZMP trajectories are shown in Fig. 15. The Y component of the COM position deviated from the desired trajectory after stepping upon the piled debris. We can also see the whole-body controller reacted against this deviation by moving the Y component of ZMP further than the COM position.

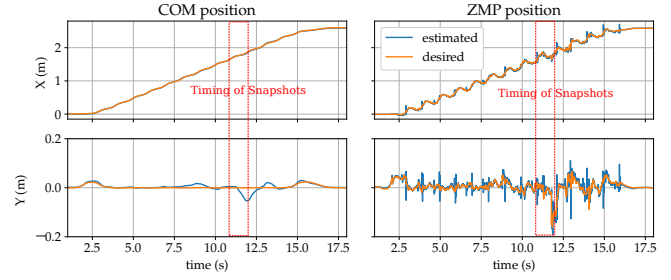


Fig. 15. COM and ZMP trajectories of trotting at 0.2 m/s on scattered debris. The area indicated by vertical red lines corresponds to pictures shown in Fig. 16. The robot was stepping on protruding debris and was leaning minus Y direction (right side of robot) around 12 seconds. Then, the robot was immediately making ZMP move largely toward minus Y direction to recover the error of COM.

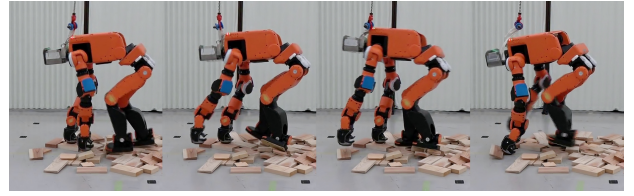


Fig. 16. Snapshots of trotting at 0.2 m/s on scattered debris. The timing is around 12 seconds of Fig. 15.

Snapshots of this timing are shown in Fig. 16.

Secondly, we tested unexpected collisions between an arm and an obstacle while trotting. We set up experiments so that the top of a hand collides with an obstacle in swing phase at maximum speed. The obstacle was aluminum and was rigidly fixed to the floor. Walking speed varied from 0.2 to 0.4 m/s. As a result, the wrist-pitch received the most severe torque load. The actual velocities of the hand and wrist-pitch torques at the time of collision are shown in Fig. 17. Snapshots of the collision at 0.4 m/s trotting are shown in Fig. 18. At 0.4 m/s trotting, the maximum torque of wrist-pitch was 120 Nm. At the time of collision, the velocity of the hand was 2.2 m/s.

Thirdly, we tested push recovery while bipedal stomping. Fig. 1(c) and the accompanying video shows the reaction of robot.

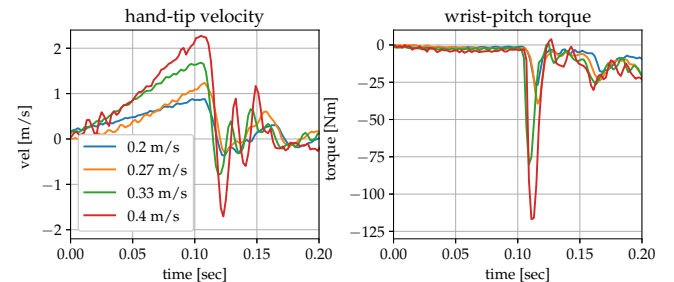


Fig. 17. Plotting of velocity of the hand and torque of the wrist-pitch joint at the time of an unexpected collision while trotting. At 0.4 m/s, torque of the wrist-pitch joint was near its limit at 125 Nm.

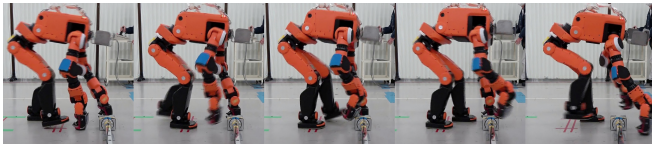


Fig. 18. Snapshots of unexpected collision while trotting at 0.4 m/s. The obstacle which the robot collided with was fixed to the floor.

IV. CONCLUSION

In this paper, we proposed new methods for compact and high performance torque-controlled actuators. A minimum axial length was achieved by placing ring-shaped torque sensors outside of motors or gears. Although this layout introduces a limitation to the choice of torque sensing devices and strong electromagnetic interference from motors to sensors, we found high fidelity torque control is possible with a custom ADC board with an analog differentiator circuit to achieve higher SNR and special configuration of the terminal board to cancel the electromagnetic interference. We also presented test results of a legged robot equipped with the proposed actuators. This robot is purely torque-controlled and can execute 0.46 m/s bipedal walking and 0.4 m/s quadrupedal walking. We demonstrated the robustness of this robot on scattered debris, against unexpected collisions and against push. In future work we plan to pursue lower stiffness of torque sensors that will make robots more tolerant against collisions. We also plan to realize variety of motions such as a ladder climbing already realized by the position-controlled version.

V. ACKNOWLEDGEMENT

We would like to thank members of the Honda R&D and the Honda Research Institute who involved in the development of the proposed system. We would also like to thank Kei Usui a former development member.

REFERENCES

- [1] S. Feng, X. Xinjilefu, C. G. Atkeson, and J. Kim, "Optimization Based Controller Design and Implementation for the Atlas Robot in the DARPA Robotics Challenge Finals," *IEEE-RAS International Conference on Humanoid Robots*, pp. 1028–1035, 2015.
- [2] D. Tsetserukou, R. Tadakuma, H. Kajimoto, and S. Tachi, "Optical Torque Sensors for Implementation of Local Impedance Control of the Arm of Humanoid Robot," *IEEE International Conference on Robotics and Automation*, 2006.
- [3] S. Shams, J. Y. Lee, and C. Han, "Compact and lightweight optical torque sensor for robots with increased range," *Sensors and Actuators, A: Physical*, vol. 173, no. 1, pp. 81–89, 2012. [Online]. Available: <http://dx.doi.org/10.1016/j.sna.2011.10.019>
- [4] N. Paine, J. Holley, G. Johnson, and L. Sentis, "Actuator Control for the NASA-JSC Valkyrie Humanoid Robot : A Decoupled Dynamics Approach for Torque Control of Series Elastic Robots," *Journal of Field Robotics*, 2014.
- [5] F. Negrello, M. Garabini, M. G. Catalano, J. Malzahn, D. G. Caldwell, A. Bicchi, and N. G. Tsagarakis, "A modular compliant actuator for emerging high performance and fall-resilient humanoids," *IEEE-RAS International Conference on Humanoid Robots*, pp. 414–420, 2015.
- [6] C. Knabe, "Design of Linear Series Elastic Actuators for a Humanoid Robot," Ph.D. dissertation, 2014.
- [7] S.-H. Hyon, D. Suewaka, Y. Torii, N. Oku, and H. Ishida, "Development of a fast torque-controlled hydraulic humanoid robot that can balance compliantly," in *IEEE-RAS International Conference on Humanoid Robots*, 2015, pp. 576–581.
- [8] K. Nagasaka, Y. Kawanami, S. Shimizu, T. Kito, and T. Tsuboi, "Whole-body Cooperative Force Control for a Two-Armed and Two-Wheeled Mobile Robot Using Generalized Inverse Dynamics and Idealized Joint Units," *IEEE International Conference on Robotics and Automation*, pp. 3377–3383, 2010.
- [9] N. G. Tsagarakis, J. Saglia, D. G. Caldwell, and Z. Li, "The Design of the Lower Body of the Compliant Humanoid Robot cCub," *IEEE International Conference on Robotics and Automation*, pp. 2035–2040, 2011.
- [10] Y. Kuroki, Y. Kosaka, T. Takahashi, E. Niwa, H. Kaminaga, and Y. Nakamura, "Cr-N Alloy Thin-film Based Torque Sensors and Joint Torque Servo Systems for Compliant Robot Control," *IEEE International Conference on Robotics and Automation*, pp. 4939–4944, 2013.
- [11] J. Engelsberger, A. Werner, C. Ott, B. Henze, M. A. Roa, G. Garofalo, R. Burger, A. Beyer, O. Eiberger, K. Schmid, and A. Albu-sch, "Overview of the torque-controlled humanoid robot TORO," *IEEE-RAS International Conference on Humanoid Robots*, 2014.
- [12] N. Kashiri, J. Malzahn, and N. G. Tsagarakis, "On the Sensor Design of Torque Controlled Actuators: A Comparison Study of Strain Gauge and Encoder-Based Principles," *IEEE Robotics and Automation Letters*, vol. 2, no. 2, pp. 1186–1194, 2017.
- [13] I. M. Kim, H. S. Kim, and J. B. Song, "Design of joint torque sensor and joint structure of a robot arm to minimize crosstalk and torque ripple," *International Conference on Ubiquitous Robots and Ambient Intelligence*, pp. 404–407, 2012.
- [14] T. Koolen, S. Bertrand, G. Thomas, T. de Boer, T. Wu, J. Smith, J. Engelsberger, and J. Pratt, "Design of a momentum based control framework and application to the humanoid robot atlas," *International Journal of Humanoid Robotics*, vol. 13, no. 1, 2015.
- [15] M. a. Hopkins and D. W. Hong, "Whole-Body Humanoid Balance Control Using Divergent Component of Motion Dynamics," *IEEE International Conference on Robotics and Automation*, pp. 1–9, 2015.
- [16] S. Kuindersma, F. Permenter, and R. Tedrake, "An Efficiently Solvable Quadratic Program for Stabilizing Dynamic Locomotion," *IEEE International Conference on Robotics and Automation*, 2014.
- [17] T. Yoshiike, M. Kuroda, and R. Ujino, "Development of Experimental Legged Robot for Inspection and Disaster Response in Plants," *IEEE/RSJ International Conference on Intelligent Robots and Systems*, 2017.
- [18] M. Osada, Y. Kanemoto, and K. Usui, "Control system for power unit," U.S. Patent 9796087, 2017.
- [19] Y. Nakayama, K. Fujikawa, and H. Kobayashi, "A Torque Control Method of Three-Inertia Torsional System with Backlash," *International Workshop on Advanced Motion Control*, pp. 193–198, 2000.
- [20] Y. Kanemoto, K. Usui, M. Osada, M. Muromachi, and S. Ogiwara, "Torque sensor terminal block structure," U.S. Patent App. 15/281 458, 2017.
- [21] N. M. Kircanski and A. A. Goldenberg, "An Experimental Study of Nonlinear Stiffness, Hysteresis, and Friction Effects in Robot Joints with Harmonic Drives and Torque Sensors," *International Journal of Robotics Research*, vol. 16, no. 2, pp. 214–239, 1997.
- [22] T. Takenaka, T. Matsumoto, and T. Yoshiike, "Real time motion generation and control for biped robot 1st report: Walking gait pattern generation," in *IEEE/RSJ International Conference on Intelligent Robots and Systems*, 2009, pp. 1084–1091.
- [23] T. Kamioka, T. Watabe, M. Kanazawa, H. Kaneko, and T. Yoshiike, "Dynamic gait transition between bipedal and quadrupedal locomotion," in *IEEE/RSJ International Conference on Intelligent Robots and Systems*, 2015, pp. 2195–2201.
- [24] M. Kanazawa, S. Nozawa, Y. Kakiuchi, Y. Kanemoto, M. Kuroda, K. Okada, M. Inaba, and T. Yoshiike, "Robust vertical ladder climbing and transitioning between ladder and catwalk for humanoid robots," in *IEEE/RSJ International Conference on Intelligent Robots and Systems*, 2015, pp. 2202–2209.